Spall damage and deformation of additive manufactured M350 steel with hierarchical structures under shock loading

ABSTRACT: This work investigates the spall damage and microstructural deformation behaviors of a heat-treated, hierarchical structured 18 wt% Ni-350 maraging steel (M350) produced by laser powder bed fusion (LPBF) under shock loading. The samples were shock-loaded along different orientations with peak shock stresses ranging from 7.0 GPa to 10.5 GPa. Experimental results demonstrate that the M350 exhibits ultra-high spall strength of 5.01 GPa-5.89 GPa and 4.53 GPa-4.99 GPa when loading perpendicularly and parallel to the building direction, respectively. Spall damage is characterized as a typical transgranular brittle fracture with {100} cleavage planes within the block. The observed superior mechanical performance is attributed to the precipitation strengthening and the transformation-induced plasticity (TRIP) effect. Specifically, the existence of the high density precipitates impedes dislocation movement according to the Orowan mechanism, preventing the formation of micro-cracks. The residual austenite undergoes martensitic phase transformation with the formation of new secondary laths with widths of 20 nm-60 nm, which creates a large number of grain boundaries and leads to grain refinement.

Keywords: spall damage; maraging steel; plate-impact experiments; transgranular brittle fracture; precipitate strengthening

1. Introduction

The 18 wt% Ni-M350 maraging steel (M350), a low carbon maraging steel, is extensively used across various industrial fields including vehicles, aerospace, and armor protection due to its remarkable combination of high strength, hardness, and superior weldability and processability[1-5]. Laser powder bed fusion (LPBF) has emerged to be a promising additive manufacturing technique to fabricate complex fine structures[6-11], addressing common challenges in traditional manufacturing methods, such as low material utilization[12-14]. Heat treatment is often necessary to mitigate residual stresses introduced during the manufacturing process and to optimize the mechanical properties of additive manufactured parts[15, 16]. For maraging steel, aging induces a martensitic transformation, resulting in a complex hierarchical structure comprising packets, blocks, and laths. Prior austenite grains are subdivided into several packets, each containing several parallel blocks. The blocks are further subdivided into parallel martensitic laths. Additionally, high-density Ni_3(Ti, Mo, Al) precipitates form within the structure[17-20]. These hierarchical structures and precipitates impede the dislocation movement, contributing to the steel's ultra-high strength[19, 21-23].

Harsh service conditions, particularly dynamic shock loading, are inevitable for M350 maraging steel in various applications. Therefore, it is crucial to understand the structural evolution and assess the material's reliability under high strain rate dynamic shock loading[24-28]. However, investigations on the mechanical behavior of the 18 wt% Ni maraging steels have largely focused on quasi-static and dynamic loading with a strain rate of less than 10^4 s^{-1}. Li et al. observed that the Fe-18Ni-5Mo-2Cr-1.2Ti-0.6V

maraging steel undergoes martensite to orthogonal transformation under quasi-static tensile loading. The stress-induced structural transformation as well as the dislocation proliferation predominate the plastic deformation[1]. Conversely, Shamsdini et al. found that 18Ni-300 maraging steel experiences martensitic transformation and grain refinement under static tensile loading[29]. At higher strain rates (10^2-10^3 s^{-1}), as the strain rate increases, strain hardening due to dislocation proliferation transitions to thermal softening driven by adiabatic shear bands. This transition leads to crack nucleation, expansion, and eventually failure[6, 7, 30, 31]. These works revealed the significant strain rate sensitivity of 18 wt% Ni maraging steel.

The dynamic deformation mechanism and damage behaviors of the M350 maraging steel remain to be elucidated for strain rates higher than 10^4 s^{-1}, though dynamic deformation and damage behaviors have been extensively investigated for other traditional steels. The damage of martensitic 1045 steel tends to nucleate at the lath or grain boundaries under impact loading, and the cracks prefer to propagate through or along the prior austenite grains, indicating a mixed cracking mode[25]. The high hardness armor (HHA) steel, however, exhibits brittle fracture characteristics[32]. Needle-like microcracks, dynamic recrystallization, and reversible BCC-HCP structural phase transition are observed in low-alloy steels as the impact pressure increases[17, 33]. The above studies only focus on the macroscopic deformations, the damage and plastic deformation mechanism of these steels are still unclear.

In this work, plate-impact experiments were carried out to investigate the spall damage and deformation behaviors of heat-treated LPBF M350. Both the macroscopic

particle velocity profile measurement and microstructural characterization of the recovered samples have been employed to understand dynamic fracture behaviors and microscopic deformation mechanisms. Experimental results reveal the superior mechanical properties of the heat-treated LPBF M350 with hierarchical structures, contributed by the interaction of precipitations and dislocation and the transformation-induced plasticity (TRIP) effect.

2. Materials and Experiments

2.1. Material & additive manufacturing processing & heat treatment

The M350 steel investigated was fabricated using the LPBF technique followed by heat treatments. The chemical compositions of the raw powders are detailed in Table 1. The powders were produced via gas atomization in a nitrogen environment[15], with an average particle diameter of ~30 μm. Printing parameters were optimized towards minimum porosity, including a laser power of 175 W, a hatch spacing of 100 μm, a layer thickness of 30 μm, and a scanning speed of 300 mm/s, resulting in an energy density of 194.4 J/mm^3. To prevent oxidation, the printing process was conducted in an argon atmosphere. A bidirectional scanning strategy and a 67° scanning rotation angle between adjacent layers were employed to reduce the accumulation of residual stress[6, 17].

As shown in Fig. 1a, the fabricated M350 material underwent heat treatment beginning with austenitization at 850 ℃ for 1 h, followed by aging treatment at 530 ℃ for 3 h. These temperature parameters were chosen based on the precipitation temperature range (450–580 ℃) and the austenite finish temperature range (450–

580 ℃)[34]. The heat treatment process was carried out in a vacuum (10^{-5} bar) to avoid oxidation. Gas quenching (nitrogen, 5 bar) with a high cooling rate (40 ℃/s) was adopted to accelerate the martensitic transformation[15].

Table 1 Chemical compositions (in wt%) of the M350 raw powders.

Element	Fe	Ni	Co	Mo	Ti	Al	C
Content	Bal.	18.44	11.91	4.88	1.45	0.12	0.01

The initial density (ρ_0) of the material was determined by the Archimedes drainage method to be 8.089 g/cm^3. Solidification processes during LPBF introduce highly textured microstructures in as-built materials[29]. To explore whether the heat-treated materials will inherit such anisotropy in terms of spall damage behaviors, spall experiments were conducted in two different directions. IP and TT denote the geometries with shock directions parallel with and perpendicular to the build direction, respectively, as presented in Fig.1b. The longitudinal sound velocity (C_L) and shear sound velocity (C_S) were measured using the ultrasonic pulse-echo method[35], and the bulk sound velocity (C_B) was then calculated via $C_B = \sqrt{C_L^2 - \frac{4}{3}C_S^2}$. Detailed parameters for both IP and TT samples are given in Table 2.

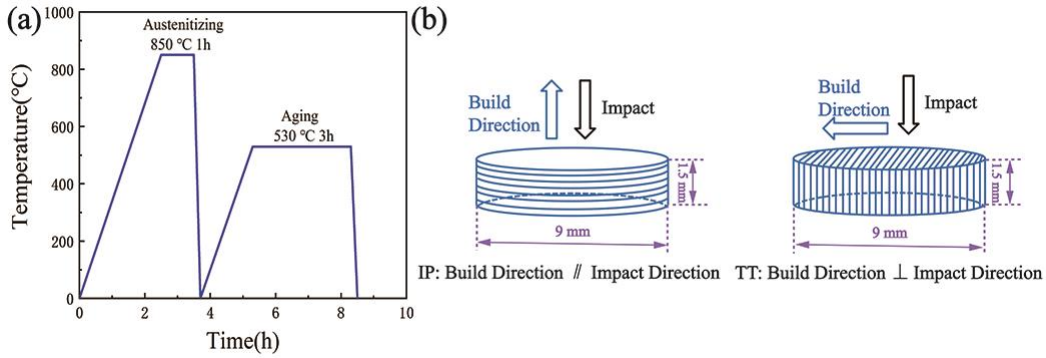


Fig. 1. (a) Thermal treatment scheme for the LPBF M350 material. (b) Geometries of impact showing two different shock directions relative to the build direction.

Table 2. Longitudinal (C_L), shear (C_S), and bulk (C_B) sound velocities for IP and TT specimens.

	C_L (m/s)	C_S (m/s)	C_B (m/s)
IP	5811	3068	4606
TT	5783	3067	4572

2.2. Plate impact experiments

Plate-impact experiments were conducted on both IP and TT samples using a single-stage light gas gun with a 14 mm bore diameter, as depicted in Fig. 2a. A flyer, made up of high-purity oxygen-free copper, was accelerated by high-pressure gases and impinged the sample at velocities ranging from 400 to 600 m/s. The flyer velocity was measured using a magnetic induction velocity measurement system[36]. The flyer dimensions were 13.0 mm in diameter and 0.75 mm in thickness, while the samples were 9.0 mm in diameter and 1.5 mm in thickness. Shock-loaded samples were recovered from a cabin filled with soft vacuum seal mud[14, 37]. Free-surface velocity (FSV) profiles were simultaneously measured using a photonic Doppler velocimeter (PDV).

Spall damages are caused by the transient tension resulting from interactions between rarefaction waves generated by the free surfaces of the sample and flyer. Upon impact, elastic waves (E_f and E_s) and plastic waves (P_f and P_s) are generated and propagate in opposite directions within the flyer and sample. When P_f and P_s reach the free surfaces of the flyer and sample, rarefaction waves (R_f and R_s) are generated and propagating towards each other, as illustrated in Fig.2b. As these two rarefaction waves encounter, intense tension is produced and spallation occurs while the tension stress exceeds the strength of the material[38, 39]. A recompression wave (S_{ra}) forms when the

rest part of R_s reaches the spall surface and gives rise to the pull-back signal in FSV profiles[17].

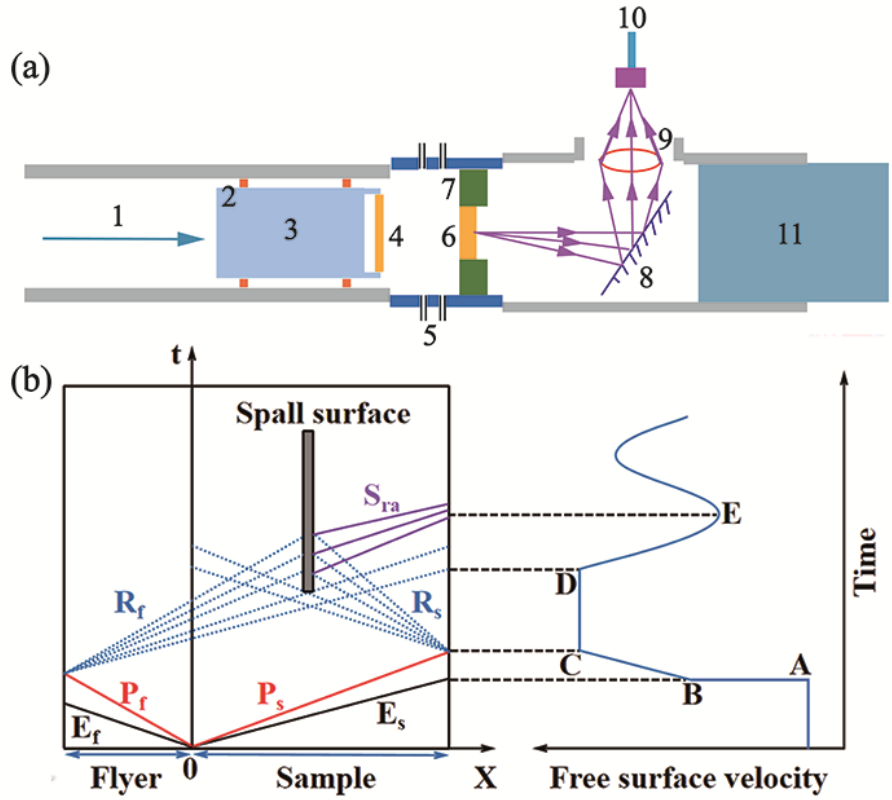


Fig.2. (a) Schematic for the spall recovery experiment. 1: high pressure gas; 2: O-rings; 3: sabot; 4: flyer; 5: magnetic velocimetry; 6: sample; 7: sample holder; 8: mirror; 9: lens; 10: optical fiber connected to the PDV; 11: soft recovery. (b) Wave interactions and free surface velocity profile. E_f and E_s: elastic waves; P_f and P_s: plastic waves; R_f and R_s: rarefaction waves; S_{ra}: recompression wave. Subscript *f* and *s* denote the flyer and sample.

2.3. Microstructure characterization

X-ray diffraction (XRD), optical microscope (OM), electron back-scattered diffraction (EBSD), and transmission electron microscopy (TEM) were utilized to characterize the microstructures of the samples at different scales, both before and after

shock loading. Samples were sectioned into two halves using the diamond wire-cutting method. For characterization, specimens were harvested from the center of the recovered sample, to minimize the effects of edge rarefaction waves. Prior to OM and EBSD characterizations, the samples were polished to a mirror finish. After that, samples were embedded in carbon resin and grounded with SiC sandpapers, and polished with diamond suspensions. EBSD characterizations were conducted using a scanning electron microscope (SEM) equipped with an Oxford Symmetry detector, with an operating voltage of 20 kV. The step size is optimized to 0.5 μm for the overall examination, and 0.2 μm for detailed investigations.

TEM was employed for nanoscale microstructure characterization. Two sample preparation methods, including the focused ion beam (FIB) and the twin-jet electro-polishing, were used. For the FIB method, ion beam thinning was performed on the litfted-out lamella to achieve a thickness of ~50 nm. Regarding the twin-jet electropolishing samples, they were first grounded down to 60 μm in thcinkennss using SiC sandpapers, and then electropolished (operated on Lebo TJ100-SE) until perforation to obtain a thin area for TEM observation. The electropolishing was carried out at a voltage of 25 V under a temperature of -32 ℃, using 10% perchloric acid and 90% methanol as electrolyte. The microstructure of the prepared samples was characterized by Tecnai G2 F20 S-TWIN at 200 kV, and energy dispersive spectroscopy (EDS) maps were carried out by Oxford EDS Inca X-Max.

3. Results and discussions

3.1. Initial microstructures

Fig. 3a and b display the inverse pole figure (IPF) maps for the initial structure of IP and TT samples, respectively. No signs of melting pools are observed due to the heat treatment[15]. The prior austenite grains exhibit a columnar morphology due to the epitaxial growth processes in LPBF manufacturing[29]. This is evident from the observed columnar and equiaxed grains for IP and TT samples, which are EBSD characterizations from different orientations.

The material exhibits a typical hierarchical structure ranging from nanoscale to microscale for martensitic steels. Similar hierarchical structures have been observed in materials such as LPBF M300[7], LPBF 24CrNiMo low-alloy steel[17], and quenched 9Ni steel[18]. Each prior austenite grain is subdivided into several packets with an average size of ~38.7 μm. A packet comprises of several parallel blocks. The blocks follow the Kurdjumov-Sachs (K-S) relationship[18, 40-43], and the average width and length are ~4–6 μm and ~29.3 μm, respectively. Such blocks can be further subdivided into laths with the same orientation and ~200–500 nm width. Dense acicular nano-precipitates are observed within the laths, and their average size is ~5 nm × 30 nm, as shown in Fig. 4a.

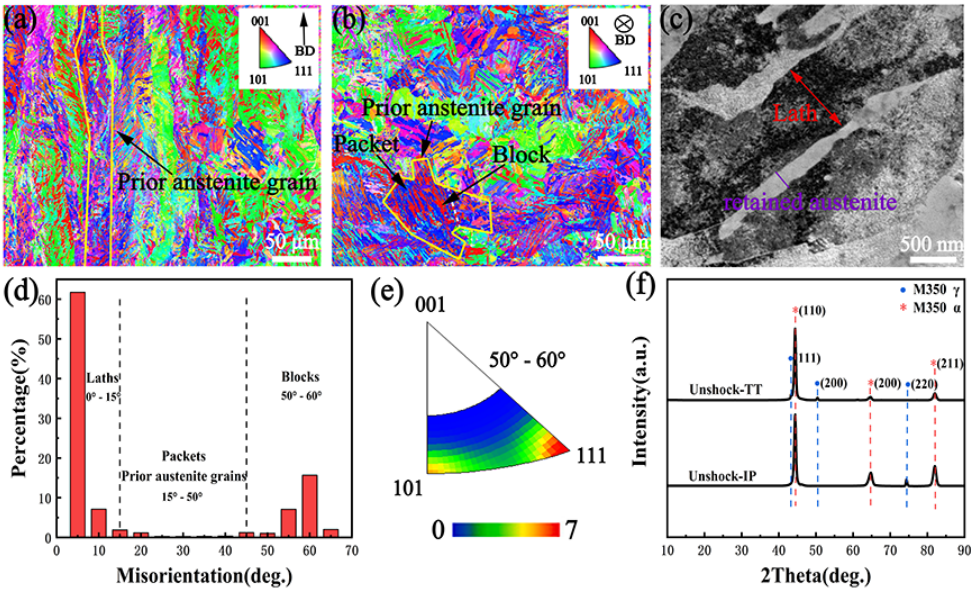
The hierarchical structure indicates the coexistence of hierarchical boundaries, including prior austenite grain boundaries, packet boundaries, block boundaries, and lath boundaries. Fig. 3d presents the distribution of misorientation angles for grain boundaries. Abundant low-angle grain boundaries (LAGBs) with 0-15° misorientation

angles can be recognized as lath boundaries, which suppress of formation and propagation of cracks, and enhance the strength of the material[41]. Grain boundaries with 15-50° misorientation angles are prior austenite grain boundaries and packet boundaries. The boundaries with 50-60° misorientation angles are block boundaries, given the fixed {112}<111> Σ3 twin boundary and <111> rotation axis as demonstrated in Fig. 3e[17, 32, 44]. The lath boundaries and block boundaries are primary low-energy boundaries, and are less prone to damage[25].

The XRD characterization results of the initial IP and TT samples are shown in Fig. 3f. Weak signals of the austenite phase (γ) are observed for both IP and TT samples, indicating the existence of a minor amount of retained austenite within the material. This is further confirmed by the TEM examinations, which reveal that retained austenite is free of precipitates and tends to form along the boundaries of martensitic lath, as shown in Fig. 3c[15].

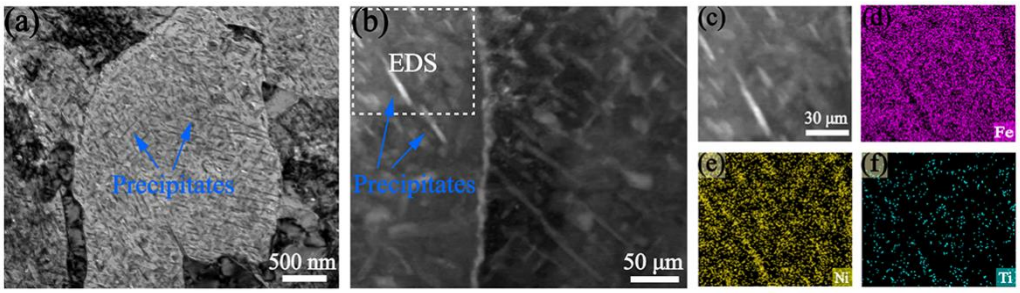
Figs. 4b-f present the EDS maps for the precipitates, showing a depletion of Fe but enrichment of Ni and Ti. These precipitates are identified as Ni_3Ti, which are commonly found in heat-treated martensitic steels. These precipitates hinder dislocation movements, which is crucial for the enhancement of steel's strength[2, 15, 21].

In general, after proper heat treatment, the LPBF-M350 exhibits a complex structure consisting of a martensitic matrix and a minor amount of residual austenite. This structure features a hierarchical arrangement of packet-block-lath and a high density of Ni_3Ti precipitates within the martensitic matrix. Fig. 5 illustrates the multi-scale structure of the material.



182

183 **Fig. 3.** Microstructural characterizations of the heat-treated LPBF M350 steels. (a) IPF
184 map of IP sample. Yellow solid box: prior austenite grain. (b) IPF map of TT sample.
185 Yellow solid box: prior austenite grain. Arrows: packet and block. (c) TEM image of
186 the laths. Red arrow: the martensite lath. Purple solid line: retained austenite. (d)
187 Histograms of grain boundary misorientation angles. (e) Inverse pole figure of the grain
188 boundaries with misorientation angle of 50-60°. (f) XRD characterization results of the
189 materials before shock loading.



190

191 **Fig. 4.** (a) TEM image of the precipitates. Blue arrows: precipitates. (b) Scanning
192 transmission electron microscopy (STEM) image of precipitates. Blue arrows:
193 precipitates. (c) Zoomed-in STEM image of the area marked by the yellow dotted

rectangle in (b). (d), (e), (f): element distributions of Fe, Ni, Ti within the region of (f), respectively.

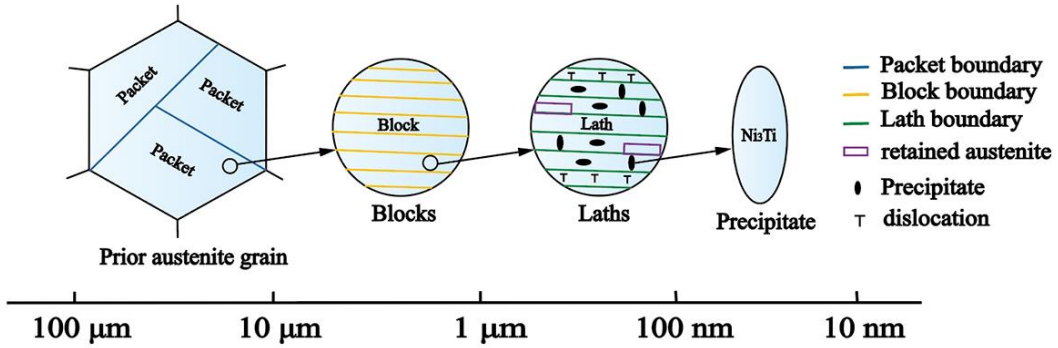


Fig. 5. Schematic of the packet-block-lath hierarchical structure of the heat-treated LPBF M350 maraging steel.

3.2. Free-surface velocity profiles

The free-surface velocity profiles for both IP and TT samples under different impact velocities are shown in Figs. 6a and 6b. All profiles exhibit a typical two-wave structure[38] with the elastic precursor (segment *AB*), Hugoniot elastic limit (HEL, point *B*), plastic wave (segment *BC*), and the stable Hugoniot state (segment *CD*). The velocity drop *DE*, also known as the pull-back signal, can be used to deduce the corresponding spall strength σ_{sp}[39, 45].

The HEL stress σ_{HEL}, peak stress σ_H, spall strength σ_{sp}, and tensile strain rate $\dot{\varepsilon}$ are obtained according to these profiles. The HEL stress σ_{HEL} is determined via[36]

$$\sigma_{HEL} = \rho_0 D_1 u_{HEL}, \quad (1)$$

where D_1 denotes the elastic wave speed, estimated as the longitudinal sound velocity (C_L). u_{HEL} is the particle velocity of the HEL and given by $u_{fs,B}/2$. The density of the sample at the compressed HEL state, ρ_{HEL}, is derived by[46, 47]

$$\rho_{HEL} = \frac{\rho_0 D_1}{D_1 - u_{HEL}}. \quad (2)$$

The peak stress σ_H can be calculated using the jump conditions[36, 46, 47]

$$\sigma_H = \sigma_{HEL} + \rho_{HEL}(D_2 - u_{HEL})(u_H - u_{HEL}), \quad (3)$$

where D_2 is the plastic wave velocity, u_H is the particle velocity at CD and can be estimated with $u_{fs,CD}/2$.

The spall strength σ_{sp} is obtained via[14, 17]

$$\sigma_{sp} = \rho_0 C_L \Delta u_{fs} \frac{1}{1 + \frac{C_L}{C_B}}, \quad (4)$$

where C_B is the bulk sound velocity. Δu_{fs} is the pullback velocity and defined as the difference between peak and minimum velocities for DE, $u_{fs,D} - u_{fs,E}$[14, 36].

The tensile strain rate during spall damage is estimated by[17, 45]

$$\dot{\varepsilon} \approx \frac{1}{2C_B} \frac{du_{fs}(t)}{dt}\Big|_{DE}, \quad (5)$$

The above-obtained parameters are summarized in Table 3. The σ_{HEL} for all shots is similar ~4.50 GPa, showing minimal dependence on the loading orientation or impact velocities. This value is significantly higher compared to typical low alloy steels such as LPBF 24CrNiMo (2.40 GPa), high hardness armor steel (2.64 GPa), and rolled homogenous armor steel (1.94 GPa)[17, 32]. The smooth elastic-plastic transition indicates the generation of a large number of initial mobile dislocations during aging or yielding[48, 49], as revealed in Fig. 6a-b.

The spall strengths of IP and TT samples at different peak stresses are shown in Fig. 6d. The spall strengths are 4.53 to 4.99 GPa for IP samples and 5.01 to 5.89 GPa for TT samples. The corresponding tensile strain rates are ~10^5 s^{-1} for all shots. The spall strengths of TT samples are slightly higher than those of IP samples[50, 51]. A similar

trend has been observed in heat-treated maraging steel C300, where TT samples give higher strength under high strain rate impact loading[7]. Besides, the spall strength of heat-treated LPBF M350 is considerably higher than those of LPBF 316L stainless steel, low-alloy martensitic steel, and typical high-entropy alloys, showing outstanding resistance to dynamic failures[17, 38, 52, 53].

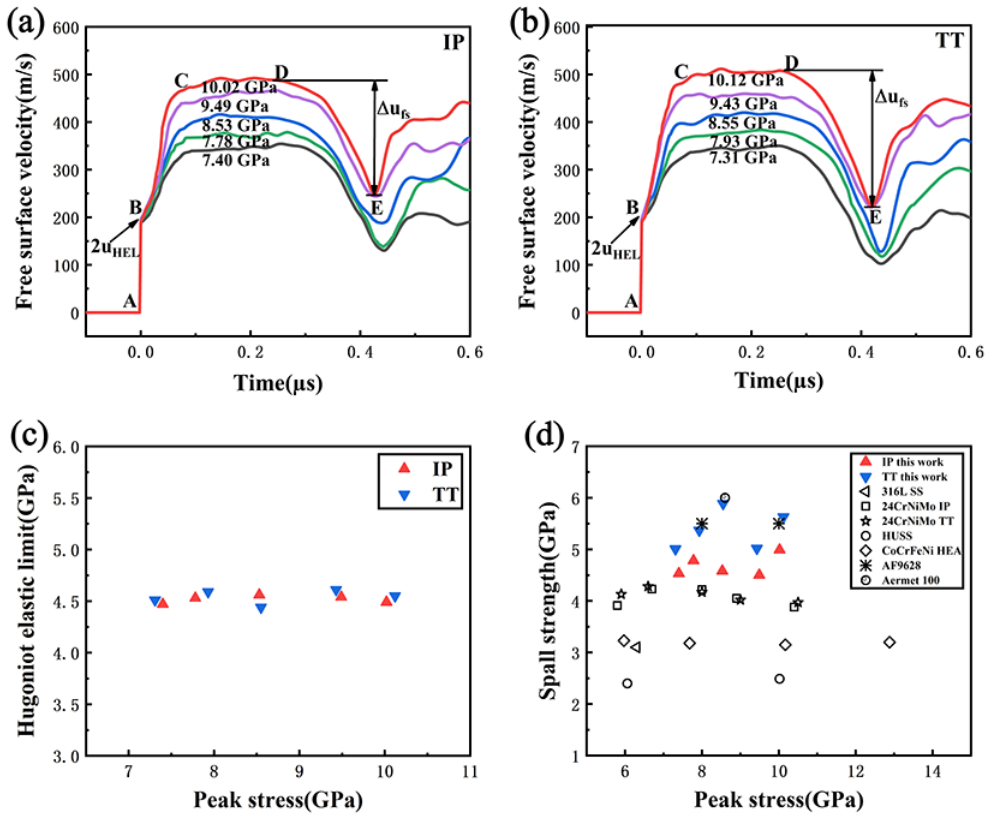


Fig. 6. (a) Free-surface velocity profiles of IP samples. (b) Free-surface velocity profiles of TT samples. (c) The HELs of IP and TT samples as a function of the peak stress. (d) Spall strength of typical materials as a function of the peak stress.

Table 3. Experimental parameters. u_f: flyer velocity; σ_{HEL}: Hugoniot elastic limit stress; ρ_{HEL}: density at Hugoniot elastic limit; σ_H: peak stress; Δu_{fs}: pullback velocity; σ_{sp}: spall strength; $\dot{\varepsilon}$: tensile strain rate.

Shot	u_f	σ_{HEL}	ρ_{HEL}	σ_H	Δu_{fs}	σ_{sp}	$\dot{\varepsilon}$

Direction	No.	(ms^{-1})	(GPa)	(g/cm^3)	(GPa)	(ms^{-1})	(GPa)	($10^5\ s^{-1}$)
IP	1	395.0	4.47	8.224	7.40	217.8	4.53	2.23
	2	415.0	4.53	8.226	7.78	230.0	4.78	2.14
	3	453.0	4.56	8.227	8.53	220.5	4.58	2.45
	4	507.6	4.54	8.226	9.49	216.3	4.50	2.49
	5	557.0	4.49	8.225	10.02	239.9	4.99	2.33
TT	6	389.0	4.51	8.227	7.31	242.4	5.01	2.42
	7	421.0	4.59	8.229	7.93	260.0	5.37	2.50
	8	459.6	4.44	8.224	8.55	285.3	5.89	2.73
	9	507.6	4.61	8.230	9.43	243.0	5.02	2.58
	10	555.0	4.55	8.228	10.12	272.8	5.63	2.33

3.3. Spallation damage behaviors

Fig. 7a and b show the cross-sectional OM micrographs of IP and TT samples subjected to different impact peak stresses. The spall damage degree evolves distinctly from incipient to complete spallation. The primary spall planes are located at the center of the samples, with similar morphologies for both IP and TT samples. As the impact pressure increases, micro-cracks grow and partially coalesce. The cracks are distributed along the shock loading direction and linked by straight and smooth shear cracks. For peak pressures higher than 10.0 GPa, the main crack forms and its width continues to increase. Branching cracks are observed near the main crack. Edge cracks on sample sides deviate from the central main crack, which can be attributed to the tensile stresses enhanced by the edge release waves.

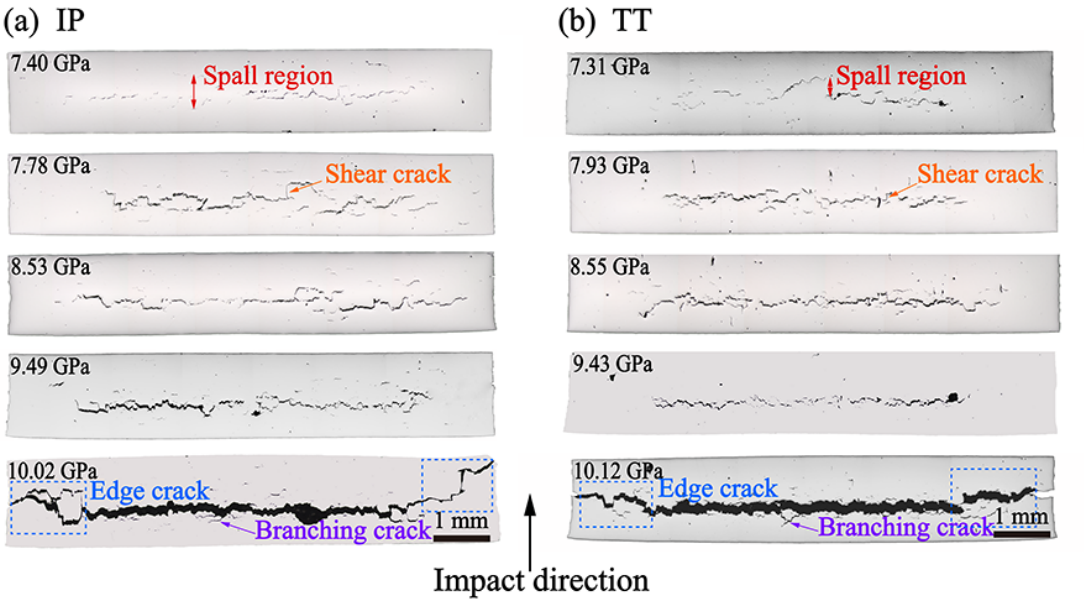


Fig. 7. Cross-sectional optical micrographs of heat-treated LPBF M350 at impact pressures ranging from 7.0 to 10.5 GPa. (a) IP samples, (b) TT samples. Red, orange, and purple arrows indicate the spall regions, shear cracks, and branching cracks. Blue dotted rectangles: edge cracks induced by edge release waves.

Figs. 8a–f present the IPF maps of postmortem IP and TT samples after shock loading. The fracture characteristics are similar in both directions. Small cracks are found at the prior austenite grain boundaries and packet boundaries. Compared to LPBF fabricated materials without heat treatment, such as 316L stainless steel[14, 38, 39, 41, 44], the cracks propagate crossing the prior austenite grains rather than along the molt pool boundaries, exhibiting a typical transgranular fracture mode. The melt pool boundaries in LPBF M350 are nearly absent, leading to damage predominantly influenced by its hierarchical structure. This mechanism is consistent with the fracture characteristics of other lath martensitic steels exhibiting zig-zag cracking patterns[17, 25, 32, 40]. Cracking is less likely to happen along LAGBs such as lath boundaries[41, 44]. The dimensions of the packets and blocks after shock loading (9.43 GPa) remain unchanged (Figs. 8g-i), so

these structures are not primarily responsible for bearing the deformation[17, 41]. Instead, structures at smaller scales such as laths and precipitates, are crucial in accommodating plastic deformations, which will be elucidated in the following sections.

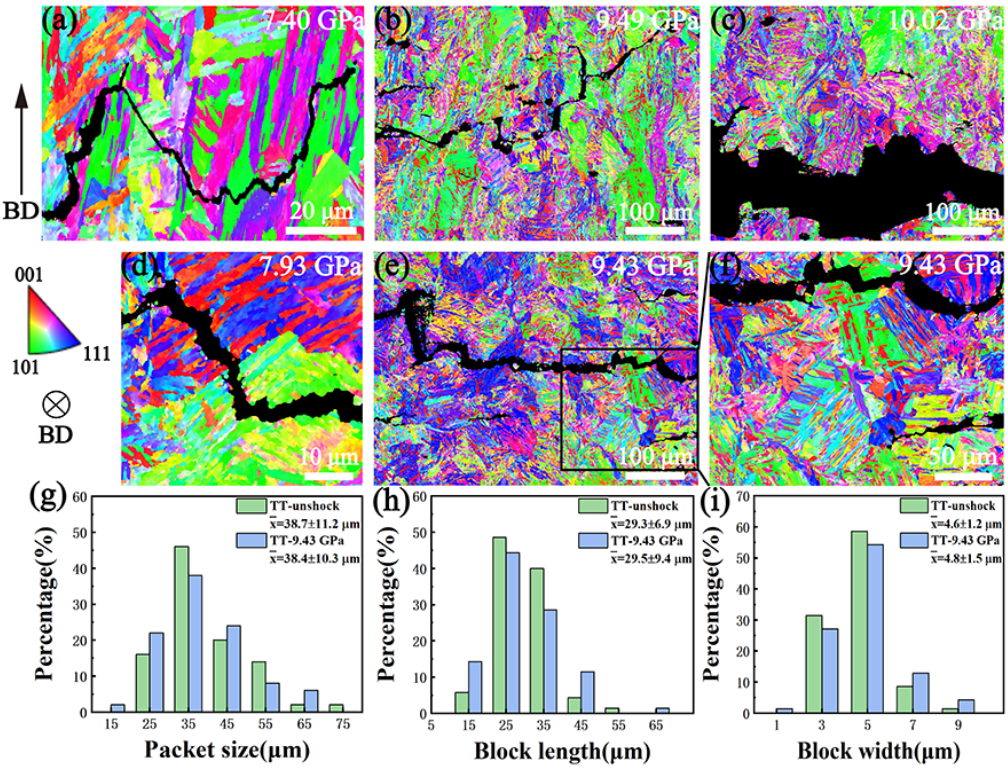


Fig. 8. Microstructural characterizations via EBSD. IPF maps of IP samples at different peak stresses: (a) 7.40 GPa, (b) 9.49 GPa, (c) 10.02 GPa. IPF maps of TT samples under different peak stresses: (d) 7.93 GPa, (e) 9.43 GPa, (f) region marked by the black rectangle in (e). Substructure dimensions of TT sample before and after 9.43 GPa shock loading. (g): packet, (h), and (i): block length and width.

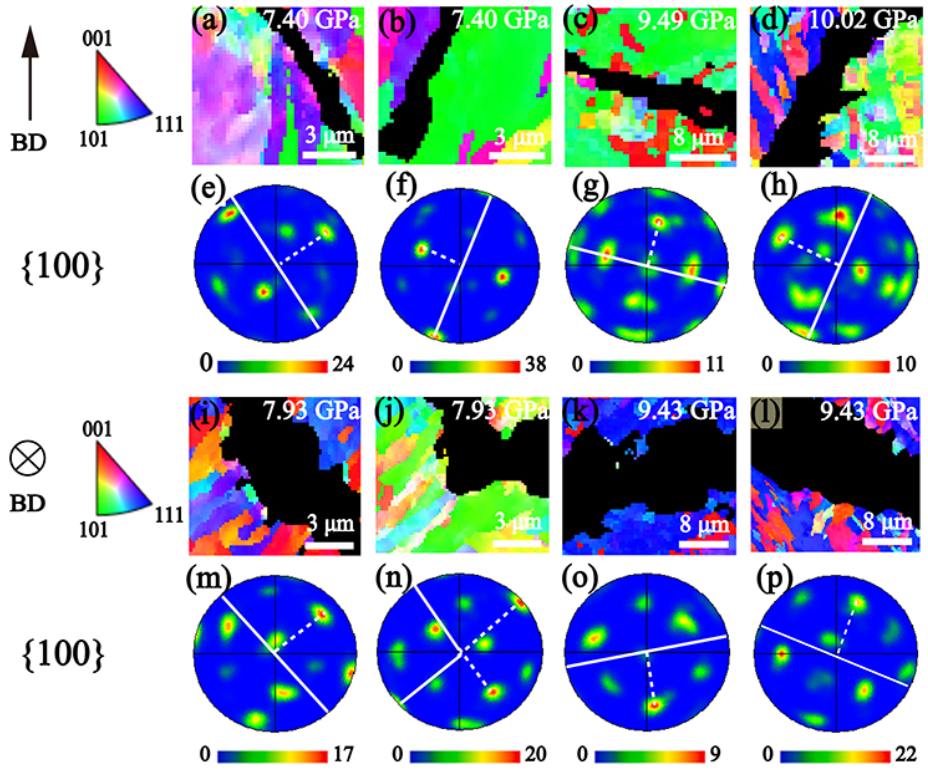


Fig. 9. (a)–(d) IPF maps of IP samples under different impact pressures. (e)–(h) The IPF maps correspond to the {100} pole figures. (i)–(l) IPF maps of TT samples under different impact pressures. (m)–(p) The IPF maps correspond to the {100} pole figures. The solid white lines in the pole figures are the projections of the cracks in the IPF maps, The white dashed lines are the normal lines of the crack projections.

The cracks traverse through the prior austenite grains and packets, and some extending across several blocks without changing direction. To reveal the correlations between the crystallographic orientations and cracking directions, cracks are projected onto pole figures as solid white lines, with normal of cracks labeled as dashed lines. These normals align with the {100} planes (red dots), suggesting a quasi-cleavage fracture along {100} planes, as shown in Fig. 9. This is consistent with the anisotropic elastic properties of martensite crystals, which exhibit a minimum Young's modulus

along [100] directions. This low Young's modulus leads to high strain localization and high vulnerability to crack initiation and propagation[2, 29].

3.4. Microstructural deformation mechanisms

Precipitation strengthening and deformation

A high density of precipitates plays a vital role in strengthening the heat-treated M350 by impeding the dislocation movement. Thus, it is natural to ask how these precipitates behave under high strain rate shock loading. Fig. 10 presents the TEM bright-field images of the nano-precipitates in postmortem samples subjected to different peak shock stresses. Abundant needle-like Ni_3Ti precipitates were observed within the martensitic laths. The distribution and morphology of the precipitates show minimal change compared to their initial state (Fig. 4a).

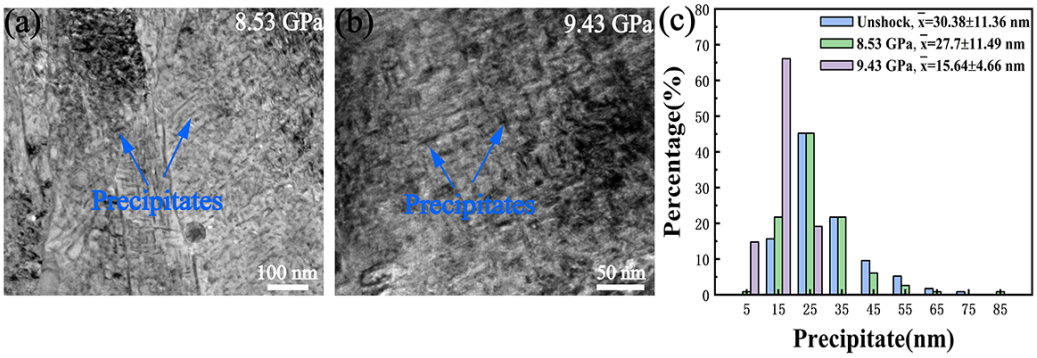


Fig. 10. TEM bright-field images of the precipitates indicated by blue arrows in postmortem samples subjected to (a) 8.53 GPa and (b) 9.43 GPa shock loading. (c) Statistical length of the precipitates for different shock stresses.

The lengths of the precipitate were analyzed and compared based on the bright-field images. As the impact stress increases, the average length of the precipitates decreases considerably. For samples shocked up to 9.43 GPa, the average length of the

precipitates is about half of its initial length. During shock loading, dislocations intersect and cut the Ni_3Ti precipitates, leading to the fracture of the precipitates, which explains the negative correlation between the precipitate length and the peak shock stress.

Due to the small size of the precipitates, there exists a small lattice mismatch at the interface between the precipitates and martensite matrix, and the elastic interaction is also mitigated. Therefore, a higher critical stress is needed to initiate the cutting processes, reducing the possibility of cracking at the precipitates-matrix interface[54]. A similar strengthening mechanism was observed in heat-treated $Al_{0.2}Co_{1.5}CrFeNi_{1.5}Ti_{0.3}$ alloy[23].

Deformation of the retained austenite

XRD profiles of the IP and TT samples before and after impact deformation are shown in Fig. 11. The weak austenite peaks in the IP and TT samples before shock loading are no longer detectable after impact, with only martensite peaks remaining. This change indicates that the retained austenite transformed into martensite during the dynamic loading process.

To further investigate the transformation mechanism, the TT sample shocked at 9.43 GPa was characterized by TEM. As shown in Figs. 12a and d, secondary laths with distinct straight boundaries and 20-60 nm width are observed within the primary laths. Fig. 12b shows a selected area electron diffraction (SAED) pattern with coexisting primary and secondary laths. There are two sets of diffraction spots corresponding to the martensite and the austenite phases. The orientations of the austenite matrix and the

secondary laths are determined to follow $[011]_\gamma//[\bar{1}11]_\alpha$ and $(\bar{1}1\bar{1})_\gamma//(\bar{1}0\bar{1})_\alpha$, which exactly matches the K-S orientation relationship[41, 42, 55].

A detailed investigation was conducted to confirm the aforementioned conclusions. Electron diffraction patterns of retained austenite along $[011]_\gamma$ zone axis and martensite along $[\bar{1}11]_\alpha$ zone axis is shown in Fig. 12c. Fig. 12e presents a high-resolution transmission electron microscopy (HRTEM) image of the boundary region. By analyzing the HRTEM image combined with the corresponding fast Fourier transform (FFT) patterns (Figs. 12f-i), the secondary laths (II) exhibit a typical martensite structure, whereas the matrix (II) retains an austenite structure. In summary, the retained austenite underwent martensitic transformation driven by the high strain rate shock loading, resulting in lamellar martensite structures and nanoscale grain refinement. Such microstructures in turn act as strong obstacles to the dislocation movement, contributing to material strengthening via the Hall-Petch effect[21, 29, 50, 53, 56]. This process exemplifies a typical TRIP process[57-60].

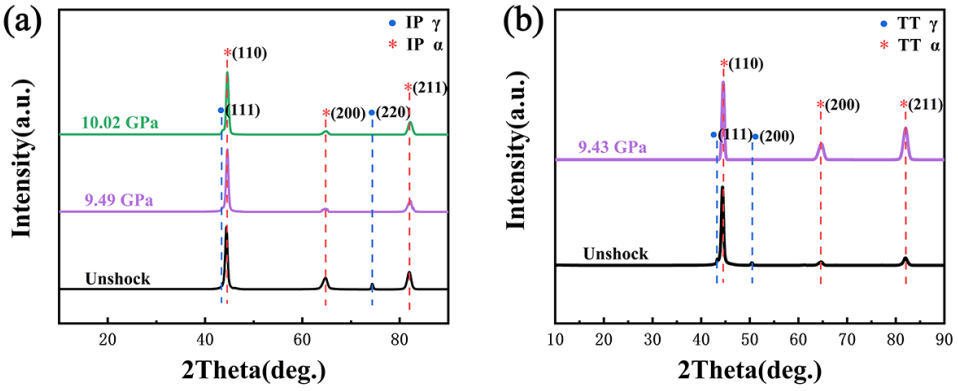


Fig. 11. XRD profiles of the IP and TT samples before and after impact.

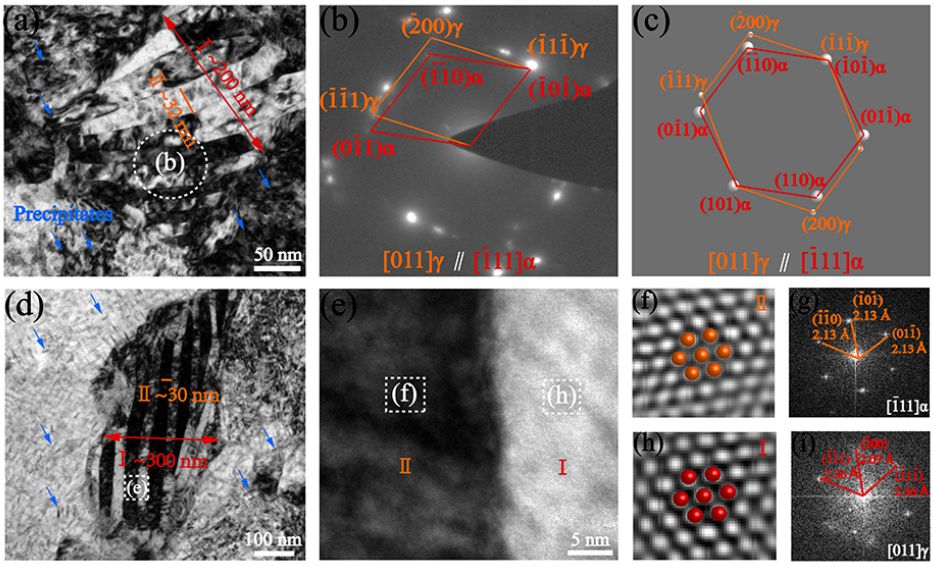


Fig.12. (a) TEM bright-field image of the secondary laths recovered sample shocked to 9.43 GPa. (b) Corresponding SAED pattern of the white dotted circle in (a). (c) Idea electron diffraction patterns with $[011]_{\gamma}//[\bar{1}11]_{\alpha}$. (d) TEM bright-field image of the secondary laths. (e) The HRTEM image of a boundary region of secondary and primary laths. (f)-(i) Zoom-in images of the boundary regions and the corresponding FFT patterns. The red and orange arrows indicate the primary γ phase laths I and secondary α phase laths II. Blue arrows indicate the precipitates.

3.5. Hierarchical damage and deformation mechanisms

The heat-treated M350 maraging steel with a hierarchical structure undergoes complex multi-scale damage and deformation behaviors under high strain rate dynamic shock loading. The spall damage is characterized by cracks propagating through the prior austenite grains, with straight and smooth shear cracks distributed along the shock direction. The cracks follow {100} cleavage planes within the blocks, with some displaying a zig-zag path indicating a transgranular brittle fracture mode.

The microstructural deformation behavior of materials involves two aspects

including the abundant precipitates distributed in martensitic matrix and retained austenite free of precipitates. For precipitates in the matrix, dislocations cut through precipitates, causing them to fracture. This process in turn hinders the dislocation movement through the Orowan mechanism, contributing to strengthening. The retained austenite, which is 200-500 nm in width and free of precipitates, undergoes martensitic transformation to form secondary martensite laths, with 20-60 nm width. This transformation results in grain refinement and the formation of numerous grain boundaries, enhancing strength through the Hall-Petch effect.

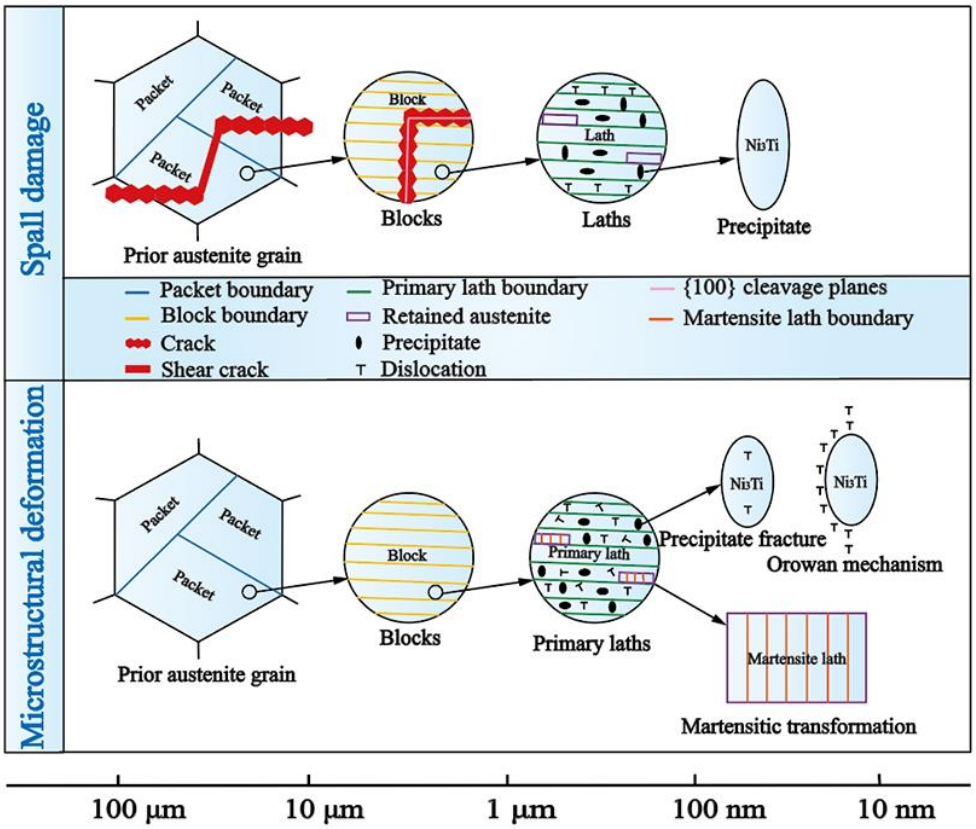


Fig. 13. Schematic illustrations of spall damage and microstructural deformation behaviors of heat-treated LPBF M350 maraging steel under high strain rate shock loading.

4. Conclusions

Plate-impact recovery experiments were conducted on heat-treated LPBF M350 maraging steel along different directions, with impact pressures ranging from 7.0 to 10.5 GPa. Free-surface velocity profiles of IP and TT samples were measured, and microstructural characterizations including OM, EBSD, and TEM were conducted on both initial and postmortem samples to explore the damage and deformation mechanisms under high strain rate loading. The main conclusions are:

(1) The Hugoniot elastic limit for IP and TT samples are similar, ~4.50 GPa. However, the spall strength shows a notable orientation dependency. The spall strength of the TT samples (5.01-5.89 GPa) is higher than that of IP samples (4.53-4.99 GPa), showing excellent dynamic mechanical properties.

(2) The damage and deformation behaviors of IP and TT samples exhibit no obvious anisotropy. Damage is characterized as typical transgranular brittle fracture, and cracks propagate along the {100} cleavage crystallographic planes within blocks.

(3) Under high strain rate impact loading, the strengthening nano-precipitates Ni_3Ti are cut by the dislocations, which in turn hinders the dislocation movement through the Orowan mechanism. The high density of the precipitates plays a vital role in the high strength of the material.

(4) Retained austenite, which is free of precipitates, undergoes martensitic transformation under dynamic loading, resulting in the formation of secondary laths with 40-60 nm widths. This transformation contributes to nanoscale grain refinement and the typical TRIP effect.

References

[1] Li H, Liu Y, Zhao W, et al. Deformation mechanism of a strong and ductile maraging steel investigated using in-situ X-ray synchrotron diffraction [J]. International Journal of Plasticity, 2023, 165.

[2] Dehgahi S, Sanjari M, Ghoncheh M H, et al. Concurrent improvement of strength and ductility in heat-treated C300 maraging steels produced by laser powder bed fusion technique [J]. Additive Manufacturing, 2021, 39.

[3] Niu M C, Chen C J, Li W, et al. Atomic-scale understanding of solute interaction effects on grain boundary segregation, precipitation, and fracture of ultrahigh-strength maraging steels [J]. Acta Materialia, 2023, 253.

[4] Duan M, Bai G, Guo S, et al. Dynamic tensile mechanical properties of 18Ni350 maraging steel fabricated by wire arc additive manufacturing [J]. Journal of Materials Research and Technology, 2023, 25: 5426-42.

[5] Asala G, Ola O T, Ojo O A. Effects of process variables on the quality and mechanical properties of 18%Ni-M350 maraging steel produced by direct energy deposition laser additive manufacturing [J]. Materials Science and Engineering: A, 2023, 866.

[6] Dehgahi S, Alaghmandfard R, Tallon J, et al. Microstructural evolution and high strain rate compressive behavior of as-built and heat-treated additively manufactured maraging steels [J]. Materials Science and Engineering: A, 2021, 815.

[7] Dehgahi S, Pirgazi H, Sanjari M, et al. Effect of building direction on high

strain-rate compressive behavior of heat-treated LPBF-maraging steels using Split Hopkinson pressure bar apparatus [J]. Materials Science and Engineering: A, 2022, 835.

[8] Zhang X X, Lutz A, Andrä H, et al. Evolution of microscopic strains, stresses, and dislocation density during in-situ tensile loading of additively manufactured AlSi10Mg alloy [J]. International Journal of Plasticity, 2021, 139.

[9] Guo L, Zhang L, Andersson J, et al. Additive manufacturing of 18% nickel maraging steels: Defect, structure and mechanical properties: A review [J]. Journal of Materials Science & Technology, 2022, 120: 227-52.

[10] Dehgahi S, Ghoncheh M H, Hadadzadeh A, et al. The role of titanium on the microstructure and mechanical properties of additively manufactured C300 maraging steels [J]. Materials & Design, 2020, 194.

[11] Wang Y, Hou Q, Li X, et al. Strain rate-dependent tensile response and deformation mechanism of laser powder bed fusion 316L stainless steel [J]. Materials Science and Engineering: A, 2024, 893.

[12] Cheng J-J, Xu C, Zhang T-Y, et al. Microstructure and dynamic mechanical behavior of wire-arc additive manufactured high-strength steel [J]. Journal of Materials Research and Technology, 2023, 25: 6099-110.

[13] Zhao Z, Wang L, Kong D, et al. Texture dependence on the mechanical properties of 18Ni300 maraging steel fabricated by laser powder bed fusion [J]. Materials Characterization, 2022, 189.

[14] Gray G T, Livescu V, Rigg P A, et al. Structure/property (constitutive and spallation response) of additively manufactured 316L stainless steel [J]. Acta Materialia,

2017, 138: 140-9.

[15] Wei S, Kumar P, Lau K B, et al. Effect of heat treatment on the microstructure and mechanical properties of 2.4 GPa grade maraging steel fabricated by laser powder bed fusion [J]. Additive Manufacturing, 2022, 59.

[16] Paul M J, Muniandy Y, Kruzic J J, et al. Effect of heat treatment on the strength and fracture resistance of a laser powder bed fusion-processed 18Ni-300 maraging steel [J]. Materials Science and Engineering: A, 2022, 844.

[17] Yang K, Chen Y, Liu X, et al. Spall properties and damage mechanisms of a low-alloy steel fabricated via laser powder bed fusion [J]. Materials Science and Engineering: A, 2022, 840.

[18] Kinney C C, Pytlewski K R, Khachaturyan A G, et al. The microstructure of lath martensite in quenched 9Ni steel [J]. Acta Materialia, 2014, 69: 372-85.

[19] Niu M C, Yin L C, Yang K, et al. Synergistic alloying effects on nanoscale precipitation and mechanical properties of ultrahigh-strength steels strengthened by Ni3Ti, Mo-enriched, and Cr-rich co-precipitates [J]. Acta Materialia, 2021, 209.

[20] Zhang H, Sun M, Liu Y, et al. Ultrafine-grained dual-phase maraging steel with high strength and excellent cryogenic toughness [J]. Acta Materialia, 2021, 211.

[21] Hadadzadeh A, Shalchi Amirkhiz B, Odeshi A, et al. Role of hierarchical microstructure of additively manufactured AlSi10Mg on dynamic loading behavior [J]. Additive Manufacturing, 2019, 28: 1-13.

[22] Niu M, Zhou G, Wang W, et al. Precipitate evolution and strengthening behavior during aging process in a 2.5 GPa grade maraging steel [J]. Acta Materialia,

2019, 179: 296-307.

[23] Ming K, Bi X, Wang J. Realizing strength-ductility combination of coarse-grained Al0.2Co1.5CrFeNi1.5Ti0.3 alloy via nano-sized, coherent precipitates [J]. International Journal of Plasticity, 2018, 100: 177-91.

[24] Li X-Y, Zhang Z-H, Cheng X-W, et al. The investigation on Johnson-Cook model and dynamic mechanical behaviors of ultra-high strength steel M54 [J]. Materials Science and Engineering: A, 2022, 835.

[25] Euser V K, Jones D R, Martinez D T, et al. The effect of microstructure on the dynamic shock response of 1045 steel [J]. Acta Materialia, 2023, 250.

[26] Hong Y, Zhang J, Wu F, et al. Coupling between phase transition and spallation in hierarchically structured high-strength martensitic steels under shock loading [J]. Engineering Fracture Mechanics, 2024.

[27] Li Z, Wang X, Hou Y, et al. Quantifying the partial ionization effect of gold in the transition region between condensed matter and warm dense matter [J]. Proceedings of the National Academy of Sciences, 2023, 120(21).

[28] Yang J, Wang X, Xu L, et al. Direct visualization of laser-driven dynamic fragmentation in tin by in situ x-ray diffraction [J]. Matter and Radiation at Extremes, 2024, 9(5).

[29] Shamsdini S, Ghoncheh M H, Sanjari M, et al. Plastic deformation throughout strain-induced phase transformation in additively manufactured maraging steels [J]. Materials & Design, 2021, 198.

[30] Truong T D, Asala G, Ola O T, et al. Effects of process parameters and loading

direction on the impact strength of additively manufactured 18%Ni-M350 maraging steel under dynamic impact loading [J]. Materials Science and Engineering: A, 2023, 874.

[31] Dehgahi S, Pirgazi H, Sanjari M, et al. Texture evolution during high strain-rate compressive loading of maraging steels produced by laser powder bed fusion [J]. Materials Characterization, 2021, 178.

[32] Wang H, Higgs S, Ameri A, et al. Spall fracture of two high strength armor steels [Z]. SHOCK COMPRESSION OF CONDENSED MATTER - 2019: Proceedings of the Conference of the American Physical Society Topical Group on Shock Compression of Condensed Matter. 2020.10.1063/12.0001024

[33] Ren J, Xu Y, Zhao X, et al. Dynamic mechanical behaviors and failure thresholds of ultra-high strength low-alloy steel under strain rate 0.001/s to 106/s [J]. Materials Science and Engineering: A, 2018, 719: 178-91.

[34] Carvalho L G D, Andrade M S, Plaut R L, et al. A dilatometric study of the phase transformations in 300 and 350 maraging steels during continuous heating rates [J]. Materials Research, 2013, 16(4): 740-4.

[35] Hu J, Zhou X, Dai C, et al. Shock-induced bct-bcc transition and melting of tin identified by sound velocity measurements [J]. Journal of Applied Physics, 2008, 104(8).

[36] Jiao Z, Li Z, Wu F, et al. Phase transition, twinning, and spall damage of NiTi shape memory alloys under shock loading [J]. Materials Science and Engineering: A, 2023, 869.

[37] Meng J, Liu Y, Li Z, et al. Investigation on the spallation properties and failure mechanism of selective laser melted Ti-6Al-4V alloy with heat treatment under shock load [J]. Journal of Alloys and Compounds, 2023, 942.

[38] Koube K D, Kennedy G, Bertsch K, et al. Spall damage mechanisms in laser powder bed fabricated stainless steel 316L [J]. Materials Science and Engineering: A, 2022, 851.

[39] Lamb K, Koube K, Kacher J, et al. Anisotropic spall failure of additively manufactured 316L stainless steel [J]. Additive Manufacturing, 2023, 66.

[40] Morris J W, Kinney C, Pytlewski K, et al. Microstructure and cleavage in lath martensitic steels [J]. Science and Technology of Advanced Materials, 2013, 14(1).

[41] Yang M, Long S-L, Liang Y-L. Study on the key role of hierarchical microstructure for strength and plasticity in a lath martensitic steel [J]. IOP Conference Series: Materials Science and Engineering, 2018, 324.

[42] Morito S, Tanaka H, Konishi R, et al. The morphology and crystallography of lath martensite in Fe-C alloys [J]. Acta Materialia, 2003, 51(6): 1789-99.

[43] Kitahara H, Ueji R, Tsuji N, et al. Crystallographic features of lath martensite in low-carbon steel [J]. Acta Materialia, 2006, 54(5): 1279-88.

[44] Liang Y, Long S, Xu P, et al. The important role of martensite laths to fracture toughness for the ductile fracture controlled by the strain in EA4T axle steel [J]. Materials Science and Engineering: A, 2017, 695: 154-64.

[45] Li C, Yang K, Tang X C, et al. Spall strength of a mild carbon steel: Effects of tensile stress history and shock-induced microstructure [J]. Materials Science and

Engineering: A, 2019, 754: 461-9.

[46] Li Y, Cao X, Yu Y, et al. Shock compression of diamonds in silicon carbide matrix up to 110 GPa [J]. Journal of Applied Physics, 2020, 128(24).

[47] Zhang W, Liu L, Ma Z-X, et al. Spall strength and equation of states for 2050-T84 Al–Li alloy under shock compression up to 120 GPa [J]. Journal of Physics and Chemistry of Solids, 2023, 174.

[48] Kositski R, Mordehai D. On the origin of the stress spike decay in the elastic precursor in shocked metals [J]. Journal of Applied Physics, 2019, 126(8).

[49] Wang Y, Tomota Y, Ohmura T, et al. Continuous and discontinuous yielding behaviors in ferrite-cementite steels [J]. Acta Materialia, 2020, 196: 565-75.

[50] Im Y-D, Kim K-H, Jung K-H, et al. Anisotropic Mechanical Behavior of Additive Manufactured AISI 316L Steel [J]. Metallurgical and Materials Transactions A, 2019, 50(4): 2014-21.

[51] Sun S-H, Koizumi Y, Kurosu S, et al. Build direction dependence of microstructure and high-temperature tensile property of Co–Cr–Mo alloy fabricated by electron beam melting [J]. Acta Materialia, 2014, 64: 154-68.

[52] Cheng J C, Qin H L, Li C, et al. Deformation and damage of equiatomic CoCrFeNi high-entropy alloy under plate impact loading [J]. Materials Science and Engineering: A, 2023, 862.

[53] Wang W, Zhang H, Yang M, et al. Shock and spall behaviors of a high specific strength steel: Effects of impact stress and microstructure [J]. Journal of Applied Physics, 2017, 121(13).

555 [54] Jiang S, Wang H, Wu Y, et al. Ultrastrong steel via minimal lattice misfit and
556 high-density nanoprecipitation [J]. Nature, 2017, 544(7651): 460-4.
557 [55] Thompson S W. Microstructural characterization of an as-quenched HSLA-
558 100 plate steel via transmission electron microscopy [J]. Materials Characterization,
559 2013, 77: 89-98.
560 [56] Sangid M D, Ezaz T, Sehitoglu H, et al. Energy of slip transmission and
561 nucleation at grain boundaries [J]. Acta Materialia, 2011, 59(1): 283-96.
562 [57] Soleimani M, Kalhor A, Mirzadeh H. Transformation-induced plasticity
563 (TRIP) in advanced steels: A review [J]. Materials Science and Engineering: A, 2020,
564 795.
565 [58] Tiamiyu A A, Eskandari M, Nezakat M, et al. A comparative study of the
566 compressive behaviour of AISI 321 austenitic stainless steel under quasi-static and
567 dynamic shock loading [J]. Materials & Design, 2016, 112: 309-19.
568 [59] Wang H, Sun X, Yang P, et al. Analysis of the Transformation-induced
569 Plasticity Effect during the Dynamic Deformation of High-manganese Steel [J]. Journal
570 of Materials Science & Technology, 2015, 31(2): 191-8.
571 [60] Chiang J, Boyd J D, Pilkey A K. Effect of microstructure on retained austenite
572 stability and tensile behaviour in an aluminum-alloyed TRIP steel [J]. Materials Science
573 and Engineering: A, 2015, 638: 132-42.
574